# Phase-Sensitive Vibrationally Resonant Sum-frequency Generation Microscopy in Multiplex Configuration at 80 MHz Repetition Rate

Hiroaki Maekawa, S. K. Karthick Kumar, Sudipta Mukherjee, and Nien-Hui Ge*

Department of Chemistry, University of California at Irvine, Irvine, California 92697-2025, United States

* To whom correspondence should be addressed.
Email address: nhge@uci.edu. Phone: 949-824-1263.

**Abstract**

Vibrationally resonant sum-frequency generation (VR SFG) microscopy is an advanced imaging technique that can map out the intensity contrast of infrared and Raman active vibrational modes with micron to submicron lateral resolution. To broaden its applications and to obtain molecular level of understanding, further technical advancement is needed to enable high-speed measurements of VR SFG microspectra at every pixel. In this study, we demonstrate a new VR SFG hyperspectral imaging platform combined with an ultrafast laser system operated at a repetition rate of 80 MHz. The multiplex configuration with broadband mid-infrared pulses makes it possible to measure a single microspectrum of $CH/CH_2$ stretching modes in biological samples, such as starch granules and type I collagen tissue, with an exposure time of hundreds of milliseconds. Switching from the homodyne- to heterodyne-detected VR SFG hyperspectral imaging can be achieved by inserting a pair of optics into the beam path for local oscillator generation and delay time adjustment, which enables self-phase-stabilized spectral interferometry. We investigate the relationship between phase images of several different C–H modes and the relative orientation of collagen triple-helix in fibril bundles. The results show that the new multiplex VR SFG microscope operated at a high repetition rate is a powerful approach to probe the structural features and spatial arrangements of biological systems in detail.

**Introduction**

Microscopic imaging based on contrasts from nonlinear interactions between electromagnetic fields and molecular vibrations has been developed as an effective approach to identify chemical species at a micrometer scale.[1-5] Nonlinear vibrational microscopy enables us to perform label-free and non-destructive measurement of specimens under ambient conditions, which is technically advantageous over fluorescence based optical microscopic methods. Moreover, nonlinear techniques have features that overcome some drawbacks of conventional Raman and Fourier transform infrared (FT IR) microscopy. For example, the signal strength in coherent anti-Stokes Raman and stimulated Raman microscopy is larger than that of Raman microscopy.[1,6] The poor spatial resolution of mid-IR imaging is highly improved in vibrationally resonant sum-frequency generation (VR SFG) microscopy,[7-21] which utilizes a nonlinear process involving an infrared-active vibrational transition and Raman-active signal generation by a tightly focused visible light. IR microscopic techniques with submicron spatial resolution were also possible based on other principles.[22-24] Applications of these nonlinear vibrational microscopy have been reported in a variety of research fields, such as life sciences, biomedical analysis, and biophotonics.

Although nonlinear microscopic images collected at a few specific wavelengths may be sufficient to shed light on certain phenomena at the microscales, to achieve a deeper understanding at molecular level requires measuring multiple bands in a wider range of vibrational microspectra. Variations in sample morphology and inhomogeneity can lead to subtle changes in peak frequency and line width that are less ambiguously revealed in a continuous spectrum than a sparsely recorded spectrum. It is, therefore, a current trend to couple microscopes with broadband light sources and to observe the spatial dependence over a significant spectral range. Hyperspectral imaging, which standardly acquires a continuous spectrum with a multichannel detector at each pixel of a scanned sample, has been experimentally implemented in nonlinear Raman microscope measurements,[25-28] and proven to be a powerful analytical tool.

To achieve hyperspectral VR SFG imaging, some prior studies have combined VR SFG spectroscopy in multiplex configuration[29-35] with a microscope setup. Multiplex VR SFG imaging systems with homodyne and heterodyne detection have been developed using ultrashort pulse lasers with a repetition ratio of kHz.[11,17,19,20] The lateral spatial resolutions of these microscopes are in the range from $1.1^{11}$ to a few $\mu m$,[17,19,20] mainly limited by the numerical aperture of objective lens and incident beam arrangement. While these microscopes are powerful, it is important to develop new approaches operating at a repetition rate higher than kHz, especially for nonlinear microscopy measurement of biological samples. For example, an intermediate repetition rate of 1–10 MHz is preferred in some cases. Two-photon excitation fluorescence microscopy at such a repetition rate enables deep tissue imaging with less photothermal damage of superficial tissues[36] and observation of fluorophores with longer lifetimes.[37] On the other hand, a high repetition rate of ~80-MHz to GHz is useful for suppressing unwanted nonlinear photodamage with low

pulse energies and for obtaining a high average intensity of nonlinear signal, as demonstrated in a second harmonic generation (SHG) microscopy study.[38] Detecting signals at a high repetition rate can reduce the dwell time needed for signal average at each pixel and hence enable fast image acquisition. Realization of hyperspectral VR SFG microscopy with a repetition rate of MHz is highly desirable because it can be employed as a valuable research tool to study biological samples. Currently, it can be carried out only by manually scanning the wavelength of narrowband mid-IR pulses[15,18] or by a more intricate system based on a sub-10-fs laser and a pulse shaper.[21] It remains as an important goal to technically demonstrate the feasibility and usefulness of multiplex VR SFG microscopy at a high repetition rate.

In this work, we construct a new VR SFG microscope with multiplex configuration based on a femtosecond Ti:sapphire oscillator and a home-built optical parametric oscillator (OPO) with a repetition rate of 80 MHz. We demonstrate that VR SFG microspectra of biological specimens, such as starch granules, can be measured with submicron lateral resolution and a subsecond acquisition time without tuning the wavelength of mid-IR light. Moreover, we enable heterodyne detection of VR SFG signal with a collinear beam geometry to significantly enhance the phase stability. We apply this technique to the structural analysis of fibrous collagen tissue and show that different C–H stretching modes exhibit different levels of sensitivity to the relative orientation. This novel microscope will be a powerful platform for chemical imaging through vibrational modes that are both IR and Raman active.

**Experimental Section**

**A. Phase-sensitive VR SFG microscope with collinear and multiplex configuration**

Figure 1a shows the schematics of the VR SFG microscope setup. Femtosecond mid-IR pulses at 3.42 μm with an 80-MHz repetition rate were generated from a home-built OPO with a periodic poled LiNbO$_3$ nonlinear crystal.[39] It was synchronously pumped by 780-nm pulses from a Ti:sapphire oscillator (Spectra-Physics, Tsunami XP) excited with a diode-pumped frequency-doubled CW laser (Spectra-Physics, Millennia eV). The conversion efficiency of the OPO is about 4%. A part of the 780-nm femtosecond pulses was sent to a 4*f* pulse shaper composed of a diffraction grating, an achromat lens, and a mechanical slit to narrow its spectral width to ∼ 1 nm, as shown in Figure 1b. Although 780 nm is typically classified as near-IR, we will refer to it as "visible" in this paper. The polarization directions of spectrally narrowed visible pulses and femtosecond mid-IR pulses were adjusted independently by a half-wave plate placed in each optical path. A pair of ZnSe wedged windows on a computer-controlled translation stage was set in the optical path of mid-IR pulses to adjust the delay time. The two excitation pulses were combined with a dichroic mirror and collinearly sent to an inverted microscope frame (Olympus, IX-73) to acquire VR SFG images by a point scanning approach. The excitation beams were focused on the sample by an aluminum coated reflective objective lens (Edmund, NA = 0.65, magnification = 74×). The sample
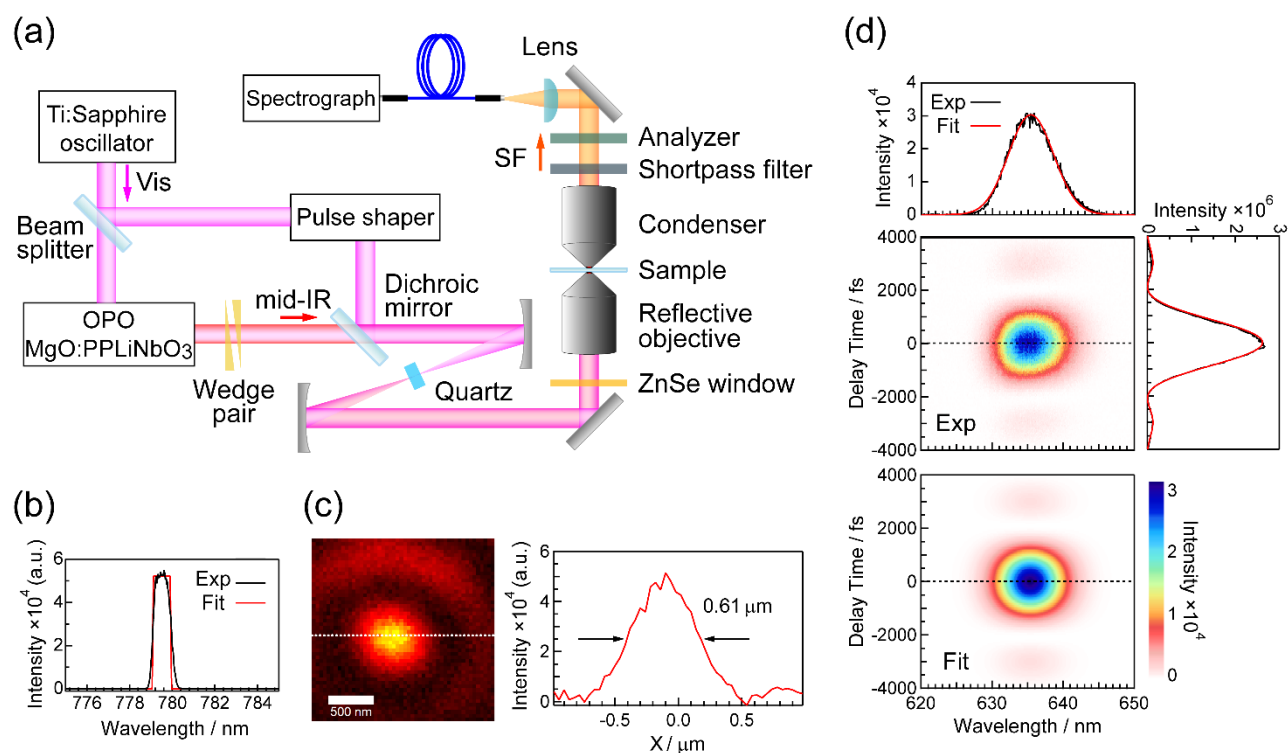
**Figure 1.** (a) Experimental setup of phase-sensitive multiplex VR SFG microscope coupled with collinear excitation light sources of an 80 MHz repetition rate. (b) The spectrum of visible pulses spectrally narrowed by a 4*f* grating-slit pulse shaper. (c) Frequency-integrated SFG image of a 300 nm diameter $BaTiO_3$ nanoparticle. The scale bar length is 500 nm. The right panel shows the intensity along a white dotted line in the acquired image. (d) Experimental and fitted 2D plots of frequency resolved cross-correlation between the visible and mid-IR pulses. The spectral slices at the delay time zero (dashed lines) are shown in the top panel. The right panel shows the delay time dependence of SF intensity integrated over the wavelength axis.

was scanned by a piezo stage (nPoint, nPBio200). The nonlinear signal generated in the forward direction was collected with a condenser and separated from the visible excitation pulse with a shortpass filter. The polarization component of the signal was selected by an analyzer. An optical fiber was used to send the signal to a spectrograph with a 1600-by-200-pixel electron-multiplying CCD camera (Princeton Instruments, ProEM Excelon) for VR SFG hyperspectral imaging. The lateral spatial resolution was estimated to be ~0.61 μm by imaging $BaTiO_3$ nanoparticles on a glass cover slip (Figure 1c). The temporal response of the multiplex VR SFG microscope was characterized by measuring the frequency-resolved cross-correlation signal from a 50-μm-thick z-cut quartz on the sample stage (Figure 1d). The measured response was fitted well by a convolution of a narrowband visible pulse with a FWHM of 16 $cm^{-1}$ and a broadband mid-IR pulse with a spectral width of 185 $cm^{-1}$.

In phase-sensitive measurements, we adopted the collinear configuration to achieve high phase stability[17,40] and generated the local oscillator (LO) before the sample.[41] The visible and mid-IR pulses were
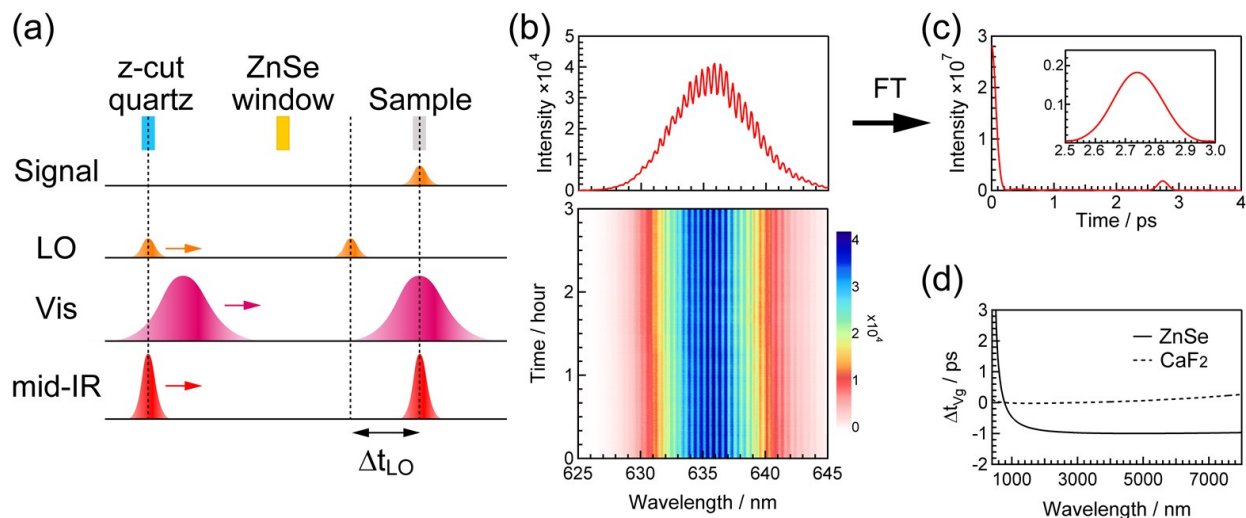
**Figure 2.** (a) Schematics to illustrate collinear heterodyne detection in the VR SFG microscope using a ZnSe window as the delay adjuster. Two snapshots in time are shown: (left) LO generation in the z-cut quartz. (right) Signal generation in the sample. The delay time between the visible and mid-IR pulses as well as the time separation between the signal and LO fields ($\Delta t_{LO}$) are adjusted by the ZnSe window. (b) Heterodyne detected interferograms of the nonresonant signal from a z-cut quartz wafer. The amplitude of Fourier transformed signal in (c) has a peak at 2.74 ps due to $\Delta t_{LO}$. (d) Wavelength dependence of the relative time lag caused by traveling through ZnSe with the unit length of 1 mm. The reference wavelength was set to 780 nm.

focused on a 50 µm thick z-cut quartz wafer using a concave mirror to generate the LO pulses. The three beams were collimated by another concave mirror and sent through a 1.59 mm thick ZnSe window before the objective lens. Here the ZnSe window serves as a delay adjuster to generate a time delay between the sample signal and the LO, $\Delta t_{LO}$ (Figure 2a). This time delay was characterized by measuring the interference between the LO and the nonresonant signal from a z-cut quartz wafer on the sample stage (Figure 2b). Fourier transform of the interference fringes shows that $\Delta t_{LO}$ is 2.74 ps (Figure 2c).

We chose ZnSe as the delay adjuster based on the following considerations. The wavelength dependence of the group velocity, $v_g(\lambda)$, and the relative time lag caused by traveling the distance of $l$ in a material with a refractive index of $n(\lambda)$,[42] $\Delta t_{v_g}(\lambda)$, are calculated below:

$$v_g(\lambda) = c/(n - \lambda \frac{\partial n}{\partial \lambda}), \quad (1)$$

$$\Delta t_{v_g}(\lambda) = l/v_g(780) - l/v_g(\lambda), \quad (2)$$

where $\lambda$ is the wavelength of light, $c$ is the speed of light in vacuum, and $l$ is set to the unit length of 1 mm. Figure 2d shows $\Delta t_{v_g}(\lambda)$ as a function of $\lambda$, indicating that mid-IR experiences a shorter time lag compared to the 780-nm light whereas the LO at 635 nm experiences a longer time lag. If the trailing edge of the visible pulse overlaps with the mid-IR pulse in the z-cut quartz to generate the LO, a 1.59-mm-thick ZnSe

window can make their peaks to coincide in time on the sample as shown in Figure 2a, and give rise to $\Delta t_{LO}$ = 2.82 ps. This calculated value is reasonably close to the measured value (Figure 2c). The stability of interference pattern was maintained at least over hours in this simple collinear beam configuration (Figure 2b). It should be noted that other mid-IR transparent materials, such as $CaF_2$, induce a much smaller time delay per unit length (Figure 2d). To cleanly extract VR SFG spectra of $CH_3/CH_2$ stretching modes from the measured interferograms, $\Delta t_{LO}$ needs to be several ps long. Therefore, a commercially available thin ZnSe window is more suitable for this purpose than a much longer optical rod.

To calibrate the homodyne and heterodyne detected data, we measured the nonresonant signal from a z-cut quartz on the sample stage as a reference and used it to normalize all of the spectra at each pixel of VR SFG images. To minimize the difference in $\Delta t_{LO}$ for the sample and reference, we carefully chose glass cover slips of the same thickness to support the tissue and quartz wafer. Heterodyne detected spectra were processed with the standard method used in SFG spectroscopic studies of interfaces[34,41] except for including an additional factor of complex number i because our measured signal originates from noncentrosymmetric regions of bulk sample. The average powers of the spectrally-narrowed visible and broadband mid-IR beams were ~ 5 and ~ 2 mW, respectively, in front of the reflective objective lens. All images were scanned over $100 \times 100$ pixels. All spectra were obtained by binning horizontal 4 pixels of the CCD output.

## B. Sample preparation

Rat tail tendon tissues were sliced and flattened between two glass cover slips to prepare collagen samples with a thickness of ~100 μm. The longitudinal axes of fiber strands were aligned parallel to the polarization direction of the excitation pulses on the sample stage. Starch granules were obtained from the surface of a sliced potato. They were suspended in water from a Milli-Q purification system, deposited on a glass cover slip, and dried up in a vacuum desiccator overnight before VR SFG microscope measurements.

## Results and Discussion

Figure 3 shows homodyne detected VR SFG microscope images and spectra of potato starch granules acquired on resonance with $CH/CH_2$ stretching modes. The polarization directions of the signal, visible, and mid-IR pulses are the same, as indicated by the arrow in Figure 3a. The exposure time at each pixel is 100 ms. The frequency-integrated intensity image clearly exhibits a lenticular shape of each granule, typically observed under an optical microscope.[43] Starch granules are mainly composed of amylose, a linear chain of α-D-(1 → 4) glucosidic linkages, and amylopectin, a highly branched glucan that has primarily α-D-(1 → 4) linkages and occasional α-D-(1 → 6) linkages that are responsible for the branching. The ratio of the two polymers varies with botanical sources: starch in potato contains about 20–30% amylose.[44,45] The structure of starch granules consists of growth rings, blocklets, and crystalline and amorphous lamellae.
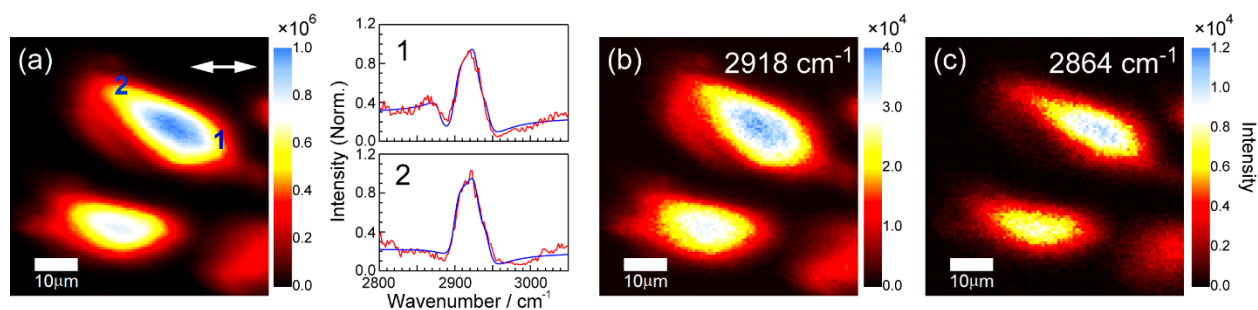
**Figure 3.** Homodyne detected VR SFG images and spectra of potato starch granules. (a) Frequency-integrated VR SFG image. The white arrow indicates the polarization direction of excitation pulses and the detected signal. Right panels show the normalized spectra measured at two different locations of the granule (red line) and spectral fittings (blue line). VR SFG images at 2918 and 2864 cm$^{-1}$ are shown in (b) and (c), respectively.

It is generally accepted that crystalline regions consist of double helices formed by short chains of amylopectin whereas amorphous regions consist of longer chains of amylopectin and probably amylose. Crystalline lamellae of native potato granules have been shown to take the B-type crystalline structure,[46] and they generate strong SHG signals[47] as well as VR SFG signals from CH and CH$_2$ modes.[48] It was also observed that VR SFG intensity spectra of research grade type III amylose powders and V-type amylose exhibit no[9] and very weak[48] peaks of CH/CH$_2$ stretching modes, respectively.

It is intriguing that different locations of a granule do not necessarily have the same VR SFG spectra of CH/CH$_2$ modes. The normalized spectrum measured at 1 in Figure 3a exhibits multiple bands in the range from 2800 to 3050 cm$^{-1}$. The peaks at 2918 and 2864 cm$^{-1}$ are clearly noticeable, with complicated lineshape. The spectrum at 1 is similar to the VR SFG spectrum of amylopectin from maize measured by Mizutani and coworkers,[9] except that our spectrum does not have a peak at ~2970 cm$^{-1}$. Kong et al. observed a strong peak at 2904 cm$^{-1}$ with a shoulder on the lower frequency side, and a weak peak at 2952 cm$^{-1}$ in VR SFG spectra for acid hydrolyzed native potato as well as for other B-type starches.[48] The origins of the former and latter peaks were assigned to the axial CH on the ring and exocyclic CH$_2$ groups, respectively. Several factors may contribute the differences of spectral shape, for example, incident angles and polarization of light fields, interference with nonresonant response, and crystallinity affected by sample preparation. In fact, when we set the polarization directions of visible and mid-IR pulses to be perpendicular with each other, the spectrum (Figure S1) exhibits peaks at 2900 and 2955 cm$^{-1}$, similar to the reported spectrum.[48] The normalized spectrum acquired at the location 2 on the same granule is similar to that measured at 1, but clearly the intensity of the apparent peak at 2864 cm$^{-1}$ is smaller. We fitted the normalized spectra by the following equation[29,32]

**TABLE 1.** Frequencies (in $cm^{-1}$) and amplitudes extracted from fitting the VR SFG spectra of potato starch measured at locations 1 and 2 on a single granule. The linewidth parameter $\Gamma_q$ was set to 10 $cm^{-1}$ for all components.

| | Location | |
|---|---|---|
| | 1 | 2 |
| $\chi_{NR}$ | 0.52 | 0.45 |
| $A_1$ at $\omega_1 = 2880$ | -2.0 | 0 |
| $A_2$ at $\omega_2 = 2900$ | 3.6 | 4.0 |
| $A_3$ at $\omega_3 = 2929$ | -4.2 | -4.2 |
| $A_4$ at $\omega_4 = 2943$ | -3.1 | -3.5 |

$$I(\omega) \propto \left| \chi_{NR}^{(2)} + \Sigma_q \frac{A_q}{\omega - \omega_q + i\Gamma_q} \right|^2, (3)$$

where $\chi_{NR}^{(2)}$ represents the nonresonant response; $A_q$, $\omega_q$, and $\Gamma_q$ are the amplitude, frequency, and line width parameter of the vibrational mode $q$ in the Lorentzian model, respectively. The spectral features are well reproduced (Figure 3a) with four peaks at 2880, 2900, 2929, and 2943 $cm^{-1}$ (Table 1 and Figure S2). Disappearance of the band at 2880 $cm^{-1}$ accounts for the difference of the two spectra reasonably well. This peak frequency is lower than those identified in FT-Raman (2911 and 2933 $cm^{-1}$) and ATR FT IR (2896, 2901 and 2926 $cm^{-1}$) spectra of commercially available amylopectin and amylose.[49] The monomer unit, α-D-glucose, exhibits well resolved peaks of CH and $CH_2$ stretching modes below 2900 $cm^{-1}$ in Raman (2883 and 2895 $cm^{-1}$) and FT IR (2855, 2877 and 2892 $cm^{-1}$) spectra, and calculation indicates that normal modes are highly delocalized over several CH bonds.[50] Hieu et at. observed a peak at 2885 $cm^{-1}$ in VR SFG spectroscopy measurement of dry α-D-glucose, and assigned it to the CH stretching mode at C(6).[51] Based on these assignments, we attribute the band at 2880 $cm^{-1}$ to a vibrational mode with a dominant contribution from the $CH_2$ stretching mode in the $-CH_2OH$ unit. Prior work on starch retrogradation[52] and cellulose[53] suggested that the $< 2900$ $cm^{-1}$ band assigned to the $CH_2$ vibration of the sugar ring is sensitive to conformational change or crystallinity of the sample. Therefore, we suggest that the spatial variation in the amplitude of the 2880 $cm^{-1}$ band is related to microscopic structure of amylopectin molecules in granules. Figures 3b and 3c show the VR SFG intensity images at 2918 and 2864 $cm^{-1}$, respectively. Figure 3b resembles the frequency-integrated Figure 3a whereas Figure 3c substantially differs from Figure 3a, demonstrating the inhomogeneous molecular environment inside granules of potato starch. Besides $CH/CH_2$ stretching modes, there are other useful vibrational modes to investigate the effects of external stimulus and hydration on starch samples.[54,55] Future application of hyperspectral VR SFG imaging in a
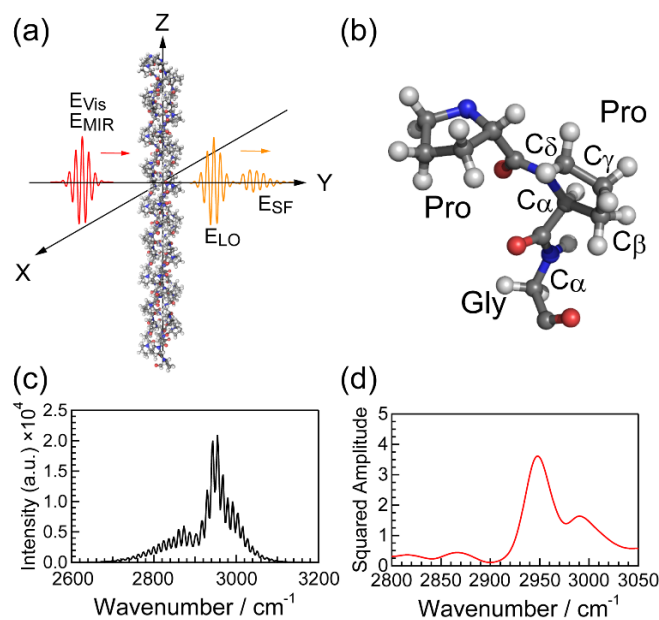
**Figure 4.** Heterodyne detected VR SFG spectrum of rat tail tendon tissue: (a) Polarization direction of incident and generated light fields and triple-helix axis orientation in the laboratory coordinate system; (b) Molecular structure of a repeating unit proline-proline-glycine in a model peptide; (c) Raw heterodyne detected interferogram; (d) Squared amplitude of the corresponding VR SFG microspectrum from (c).

wide range of wavelengths will enable further insights into the details of granules with a sub-micron spatial resolution.

We explored the usefulness of heterodyne detected multiplex VR SFG microscopy by applying it to type I collagen fibers in rat tail tendon tissues. The collinear and multiplex configuration enabled us to acquire hyperspectral images with more reliable phase stability than the method of scanning the wavelength of narrow band mid-IR pulse and overlapping the signal with the LO field passing through an external optical path, as performed in our previous study.[14] The type I collagen molecule takes a triple helical structure (Figure 4a) composed by polypeptide chains with repeating units X-Y-Gly, where the residues X and Y are often occupied by proline or hydroxyproline (Figure 4b).[56] Figures 4c and 4d show an example of heterodyne detected interferogram and the corresponding VR SFG spectrum of collagen tissue sample, respectively. We detected a strong peak at 2948 cm$^{-1}$ and several additional peaks at 2991, 2867, and 2816 cm$^{-1}$. The spectral shape is almost identical to that measured for native type I collagen fibrils by transmission VR SFG spectroscopy with PPP polarization configuration.[57] In that study, the band at 2949 cm$^{-1}$ is assigned to the Fermi resonance between the symmetric stretching and bending overtone modes of $CH_2$ group, and the band at 2994 cm$^{-1}$ is assigned to the asymmetric $CH_2$ stretching mode.

VR SFG amplitude images (Figure 5, top), acquired with an exposure time of 250 ms, and mapped out at the peak frequencies, clearly exhibit aligned fibrillar strands of collagen. Besides the signal strength
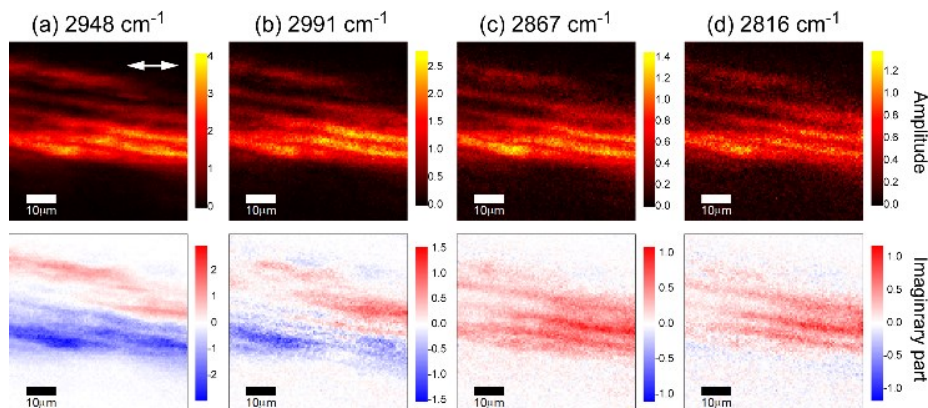
**Figure 5.** Heterodyne detected VR SFG images of rat tail tendon tissue. Amplitude (top) and imaginary part (bottom) of VR SFG spectra at (a) 2948, (b) 2991, (c) 2867, and (d) 2816 cm$^{-1}$ are mapped out. The white arrow in (a) indicates the polarization direction of the excitation and the detected signal fields.

difference between images, there is no noticeable frequency dependence. On the contrary, images plotting the imaginary part of processed interferometric data (Figure 5, bottom) reveal a change in phase and a clear frequency dependence. In the images at 2948 and 2991 cm$^{-1}$, the area of the same phase has a width of about 15–20 μm and is elongated along the direction of fiber strands. The same kind of phase flip was also detected at 2950 cm$^{-1}$ in our previous VR-SFG microscopic study using narrow band mid-IR pulses,[14] and an interferometric SHG microscopy study by Légaré and coworkers.[58] In the experimental configuration of Figure 4a, where the rat tail tendons are oriented along the Z axis of the laboratory coordinate system and the incident and detected light fields are also polarized along the same direction as the fiber axis of collagen, the second-order nonlinear susceptibilities of CH$_2$ symmetric and asymmetric stretching modes are described by eqs 4 and 5, respectively:[32,59]

$$\chi^{(2)}_{ZZZ,\mathrm{CH_2ss}} = N_{\mathrm{CH_2ss}}\big[\langle \sin^2\psi\rangle\beta^{aac}_{\mathrm{CH_2ss}} + \langle\cos^2\psi\rangle\beta^{bbc}_{\mathrm{CH_2ss}}\big]\langle\cos\theta\rangle$$
$$- N_{\mathrm{CH_2ss}}\big[\langle\sin^2\psi\rangle\beta^{aac}_{\mathrm{CH_2ss}} + \langle\cos^2\psi\rangle\beta^{bbc}_{\mathrm{CH_2ss}} - \beta^{ccc}_{\mathrm{CH_2ss}}\big]\langle\cos^3\theta\rangle, (4)$$

$$\chi^{(2)}_{ZZZ,\mathrm{CH_2as}} = 2N_{\mathrm{CH_2as}}\beta^{aca}_{\mathrm{CH_2as}}\langle\sin^2\psi\rangle\big[\langle\cos\theta\rangle - \langle\cos^3\theta\rangle\big], (5)$$

where $N_{\mathrm{CH_2ss\,(CH_2as)}}$ and $\beta^{ijk}_{\mathrm{CH_2ss\,(CH_2as)}}$ $(i,j,k = a,b,c)$ are the number and the hyperpolarizability tensor component in the molecular fixed coordinate system $(a,b,c)$ for CH$_2$ symmetric (asymmetric) stretching mode, respectively. The two coordinate systems are connected by the Euler angles, $\theta$ and $\psi$, as defined in Figure S3a, and their orientational average is represented by the bracket operator in eqs 4 and 5. These

equations are valid under the assumption that the $CH_2$ groups are azimuthally symmetric around the fiber axis, represented by the other Euler angle $\phi$. We analyzed the structure of a model collagen triple helix peptide [(Pro-Pro-Gly)$_{10}$]$_3$ determined by the X-ray diffraction (PDB code: 1K6F)[60] and found that the $CH_2$ groups of proline rings and glycine show a random orientation of $\phi$ (Figure S4). The analysis also indicates that $\theta$ and $\psi$ have a limited angle distribution in helical chains, and hence it is not adequate to further simplify eqs 4 and 5 by assuming isotropic rotation for these angles. When the fiber orientation is rotated by 180° from the Z axis, the angles $\theta$ and $\psi$ are converted to $(\pi - \theta)$ and $(\psi + \pi)$, respectively; the sign of $\chi^{(2)}_{ZZZ,CH_2ss}$ and $\chi^{(2)}_{ZZZ,CH_2as}$, in the equations is flipped and revealed in the phase resolved VR SFG images in Figure 5a,b. The phase flips of both symmetric and asymmetric $CH_2$ modes are theoretically explained, and hence we consider that the domains with different phases in Figure 5a,b reflect the relative orientation of collagen fiber bundles. In a recent study of nonlinear optical Stokes ellipsometric microscopy with ab initio calculations, it was proposed that roughly half of collagen fibrils are antiparallel with the fiber axis.[61]

In contrast, the images at 2816 and 2867 cm$^{-1}$ in Figures 5c,d exhibit the same phase over almost the whole scanned region of collagen tissue. The two weak bands between 2800 and 2900 cm$^{-1}$ observed for the collagen sample have not been clearly assigned to specific vibrational modes in the literature. In FT IR spectral analysis of a collagen model dipeptide, L-prolyl-L-hydroxyproline, some peaks below 2900 cm$^{-1}$ were reported under the $CH_2$ ring modes without clear attributions.[62] The proline and hydroxyproline residues have CH groups on $C_\alpha$, and the stretching mode may contribute to the VR SFG spectrum. In previous VR SFG studies of polymers, some peaks observed in 2850–2910 cm$^{-1}$ range were assigned to the CH stretch.[63,64] The second-order nonlinear susceptibility of this mode with $C_{\infty v}$ symmetry is described as[32,59]

$$\chi^{(2)}_{ZZZ,CH} = N_{CH}[\beta^{aac}_{CH}\langle\cos\theta\rangle + (\beta^{ccc}_{CH} - \beta^{aac}_{CH})\langle\cos^3\theta\rangle]\,,(6)$$

where $N_{CH}$ and $\beta^{ijk}_{CH}$ are the number and the hyperpolarizability tensor of CH mode, respectively. When $\theta$ is replaced with $(\pi - \theta)$, $\chi^{(2)}_{ZZZ,CH}$ also reverses its sign, just like those in eqs 4 and 5. Therefore, assigning 2867 cm$^{-1}$ to the CH stretch cannot explain the uniform phase sign in the collagen tissue observed in Figure 5c.

According to amino acid composition analysis of type I collagen from rat tail tendon, alanine exists more frequently (10.53%) than any other residues (< 5%), following glycine (33.22%) and proline / hydroxyproline (21.96%).[65] The peaks at 2816 and 2867 cm$^{-1}$ may be assigned to the C–H stretching modes of $CH_3$ and $CH_2$ groups in side chains of alanine and other residues. For example, Kaplan and coworkers measured FT IR spectra of a type I collagen film and assigned the peak at 2876 cm$^{-1}$ to $CH_3$ stretching modes of side chains.[66] However, $\chi^{(2)}_{ZZZ}$ of the $CH_2$ and $CH_3$ stretching modes does not have terms that

include even functions of $\theta$, such as $\langle\cos^2\theta\rangle$, no matter how they are orientated around the helical axis. Therefore, the localized $CH_2$ mode with $C_{2v}$ symmetry or $CH_3$ mode with $C_{3v}$ symmetry would always exhibit the phase flip as explained above. This is not consistent with the observed phase images in Figures 5c,d.

One important factor to consider is the distribution of the helical axis in collagen fibril bundles. Indeed, several previous studies, including SHG microscopy[67] and NMR,[68] reveal that collagen triple-helices are oriented at a tilt angle from the fibril axis, where the mean tilt angle is about 2–5° and the standard deviation is around 12–19° for tendons. The tilted helical axis will affect the orientational average in eqs 4–6 and smear out the clear phase flipping expected for the CH and $CH_2$ modes in antiparallel fibrils. This effect will be more significant for vibrational modes having the Euler angle $\theta$ close to 90°, compared to modes with a small $\theta$, as schematically illustrated in Figure 6. When a mode in a triple helix is pointing nearly perpendicular to the helical axis, eqs 4–6 may keep the same sign in another antiparallel helix if the tilt angle $\alpha$ is sufficient to make $(\pi - \theta - \alpha)$ less than 90° (Figure 6b). Therefore, the phase information from such a mode cannot indicate the relative orientation of collagen fibers. As shown in Figure S4, $C_\alpha H$ and $C_\gamma H_2$ of proline residues, and $C_\alpha H_2$ of glycine residues have $\theta \sim 90°$ in the $[(Pro\text{-}Pro\text{-}Gly)_{10}]_3$ model triple helix.[60] Interestingly, Dong and coworkers reported 94.8° as $\theta$ averaged for all pyrrolidine $CH_2$
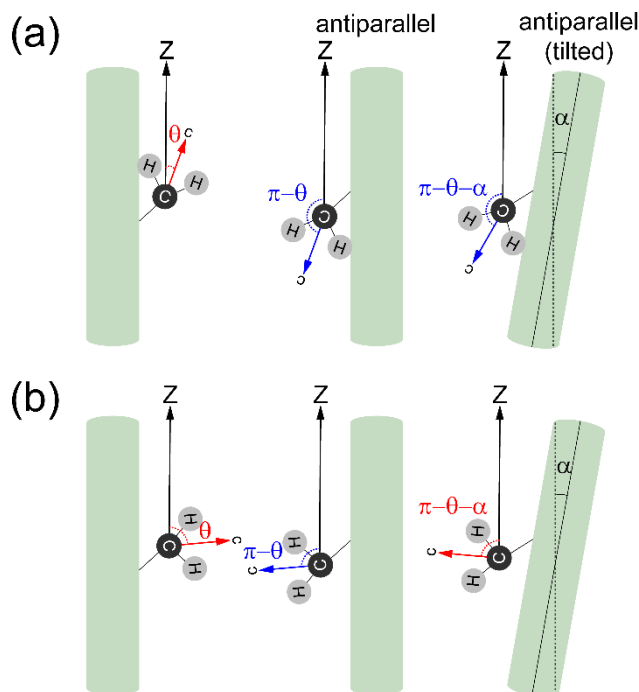


**Figure 6.** Schematics to illustrate how the sign of eqs 4,5 is affected by the orientation and tilt angle ($\alpha$) of collagen triple-helix (green cylinder). (a) When $\theta$ is small, a sign change will result from arranging the triple-helix in the antiparallel orientation with or without tilting [$(\pi - \theta)$ and $(\pi - \theta - \alpha)$ are both larger than 90°]. (b) When $\theta$ is close to 90°, antiparallel orientation with tilting may give rise to no sign change [$\theta$ and $(\pi - \theta - \alpha)$ are both less than 90°].

groups in type I collagen from rat tail tendon based on polarization-resolved SHG microscopy measurements.[69] On the other hand, the $CH_2$ modes which are not perpendicular to the helical axis, such as $C_\beta H_2$ and $C_\delta H_2$, are less sensitive to small tilting (Figure 6a), and hence phase sensitive VR SFG measurements of these modes can probe the different signs resulting from fiber orientation more clearly. Previous VR SFG signals of collagen probed at 2882 cm$^{-1}$ exhibit very different polarization dependence from that at 2949 cm$^{-1}$, suggesting that these bands have different molecular origins and spatial arrangements.[14] Taken all together, we can tentatively associate Figure 5c with $CH_2$ modes having a $\theta$ close to 90° (Figure 6b), whereas Figures 5a,b can be associated with $CH_2$ modes having a small $\theta$ (Figure 6a).

Another consideration is that for large biological molecules like collagen, it is less likely that a spectral band can be exclusively attributed to the C–H stretching mode of one specific CH, $CH_2$, or $CH_3$ group in amino acid residues. Also, some combination of $CH_2$ stretching modes of pyrrolidine rings may contribute to the observed bands in this frequency range. Somorjai and coworkers detected a peak at 2875 cm$^{-1}$ in the VR SFG spectrum of L-proline on $d_8$-polystyrene, and attributed its origin to a combination of $C_\beta H_2$, $C_\gamma H_2$ and $C_\delta H_2$ symmetric stretching modes.[70,71] For coupled vibrators in the collagen triple helix, the symmetry of the hyperpolarizability tensor is not as simple as $C_{2v}$ of a single $CH_2$ group. In this case we will not be able to rely on eqs 4 and 5 to predict the relationship between the phase of VR SFG signal and fiber orientation; further vibrational analysis and theoretical treatment will be needed.

In chemical analysis based on microspectra, a high frequency resolution is preferred. The frequency resolution of the VR SFG microscope developed in this study is limited by the spectral width of visible pulses (Figure 1b). The width of the mechanical slit in the 4$f$ pulse shaper could be further narrowed at the sacrifice of the incident power to the microscope. To optimize the SFG signal strength and frequency resolution, it would be beneficial to replace the fixed-ratio beam splitter in Figure 1a with, for example, a combination of half-wave plate and polarizing beam splitter to enable continuous adjustment of the power ratio between pumping the OPO and going through the pulse shaper. We expect that this method can increase the current frequency resolution, at least, by a factor of 2. Another way to achieve further improvement is to perform high resolution broadband SFG spectroscopy by synchronized femtosecond and picosecond laser systems, as innovated by Wang and coworkers.[72]

The total acquisition time of a VR SFG hyperspectral image using the current experimental scheme is mainly determined by the exposure time on the CCD camera at each pixel. The multiplex configuration allows us to obtain hyperspectra from a specific sample position with significantly better signal-to-noise ratio and is much faster than the wavelength scanning method without concerns to maintain spatial overlap of visible and mid-IR pulses.[73] However, if we want to simply acquire a VR SFG image at a specific wavelength, the new multiplex scheme takes a longer time than the previous method.[12] This drawback can be overcome by directing the frequency-dispersed signal to another detection port on the monochromator

and measuring the intensity through a slit by a photo multiplier tube while scanning the sample. Data collection time for one image will be significantly reduced, to an order of a minute, similar to what we recorded previously for the same sample.[12] The multiplex system with two detection ports will be very versatile for VR SFG hyperspectral imaging. The multiplex configuration with collinear excitation beams and LO is especially superior for phase sensitive measurements over a wide spectral range. Retrieving the phase through spectral interferometry eliminates the need to modulate the phase of LO via a modulator. In the first phase-sensitive SFG spectroscopy work using narrowband pulses,[74] the excitation and LO beams are collinear and passing through a phase modulator. A minimum of four spectral scans is necessary to achieve phase measurement over a wide spectral range.[74] In our previous phase-sensitive VR SFG microscope,[14] the excitation beams were split to generate LO in a separate optical arm and the LO phase was modulated by an electro-optical modulator before it was recombined with the excitation beams. This scheme requires two measurements to determine the phase; and the phase stability can only be maintained for a short time (~ 2 min). It took 40 min of equipment time to acquire 20 images each for the real and imaginary parts and average them to get the phase-resolved images at a single wavelength in ref 14, whereas the images in Figure 5 were acquired in 42 min of equipment time and the data contains 400 different wavelength points. Collinear LO generation, as implemented in our new microscope, guarantees superior phase stability over a long data acquisition time. It also greatly simplifies the alignment procedure.

Some interesting properties that can be investigated in the future are the focal depth and optical sectioning of VR SFG microscopy. We are able to observe heterodyne detected signals from rat tail tendon tissues of ~100 μm thickness. However, we expect the maximum sample thickness to be limited due to the penetration and scattering of excitation beams and induced SFG signal and LO field in the forward detection.

**Concluding remarks**

In conclusion, we have constructed a new heterodyne detected multiplex VR SFG microscope coupled with excitation pulses at an 80-MHz repetition rate and performed hyperspectral imaging with submicron spatial resolution. We have demonstrated that a commercially available thin ZnSe window is sufficient to adjust the timing between the signal and LO fields in spectral interferometric measurements. VR SFG hyperspectra of $CH/CH_2$ stretching modes in biological samples, such as starch granules and type I collagen fibers, can be recorded with an acquisition time of less than a second without scanning the wavelength of mid-IR light. Our results show that the C–H stretching modes in VR SFG spectra are sensitive reporters that can be used to investigate local molecular structure and fiber orientation. Broadband mid-IR pulses at longer wavelengths can be generated by nonlinear optical conversions such as difference frequency generation, and hence the experimental scheme demonstrated in this work will be widely applicable to other vibrational modes in the fingerprint region without further technical modifications.

Hyperspectral VR SFG microscopy is a powerful approach to enrich our knowledge of microscopic aspects in structural biology and a variety of research fields.

## Supporting Information

The Supporting Information is available free of charge.

A VR-SFG microspectrum of starch granules acquired with perpendicular polarization configuration; absolute-square spectra of the resonant Lorentzian components with the fitting parameters listed in Table 1; the definition of Euler angles and the molecule-fixed coordinate system that specifies the orientation of $CH_2$ and CH groups; and the Euler angles calculated for the three chains of a collagen triple helix model peptide.

## Acknowledgments

## References

(1) Krafft, C.; Dietzek, B.; Popp, J. Raman and CARS Microspectroscopy of Cells and Tissues. *Analyst* **2009**, *134*, 1046-1057.

(2) Min, W.; Freudiger, C. W.; Lu, S.; Xie, X. S. Coherent Nonlinear Optical Imaging: Beyond Fluorescence Microscopy. *Annu. Rev. Phys. Chem.* **2011**, *62*, 507-530.

(3) Chung, C.-Y.; Boik, J.; Potma, E. O. Biomolecular Imaging with Coherent Nonlinear Vibrational Microscopy. *Annu. Rev. Phys. Chem.* **2013**, *64*, 77-99.

(4) Zumbusch, A.; Langbein, W.; Borri, P. Nonlinear Vibrational Microscopy Applied to Lipid Biology. *Prog. Lipid Res.* **2013**, *52*, 615-632.

(5) Li, R.; Wang, X.; Zhou, Y.; Zong, H.; Chen, M.; Sun, M. Advances in Nonlinear Optical Microscopy for Biophotonics. *J. Nanophotonics* **2018**, *12*, 1-13.

(6) Petrov, G. I.; Arora, R.; Yakovlev, V. V.; Wang, X.; Sokolov, A. V.; Scully, M. O. Comparison of Coherent and Spontaneous Raman Microspectroscopies for Noninvasive Detection of Single Bacterial Endospores. *Proc. Natl. Acad. Sci. U.S.A.* **2007**, *104*, 7776.

(7) Flörsheimer, M.; Brillert, C.; Fuchs, H. Chemical Imaging of Interfaces by Sum Frequency Microscopy. *Langmuir* **1999**, *15*, 5437-5439.

(8) Kuhnke, K.; Hoffmann, D. M. P.; Wu, X. C.; Bittner, A. M.; Kern, K. Chemical Imaging of Interfaces by Sum-Frequency Generation Microscopy: Application to Patterned Self-Assembled Monolayers. *Appl. Phys. Lett.* **2003**, *83*, 3830-3832.

(9) Miyauchi, Y.; Sano, H.; Mirzutani, G. Selective Observation of Starch in a Water Plant Using Optical Sum-Frequency Microscopy. *J. Opt. Soc. Am. A* **2006**, *23*, 1687-1690.

(10) Cimatu, K. A.; Baldelli, S. Chemical Microscopy of Surfaces by Sum Frequency Generation Imaging. *J. Phys. Chem. C* **2009**, *113*, 16575-16588.

(11) Inoue, K.; Fujii, M.; Sakai, M. Development of a Non-Scanning Vibrational Sum-Frequency Generation Detected Infrared Super-Resolution Microscope and Its Application to Biological Cells. *Appl. Spectrosc.* **2010**, *64*, 275-281.

(12) Raghunathan, V.; Han, Y.; Korth, O.; Ge, N.-H.; Potma, E. O. Rapid Vibrational Imaging with Sum Frequency Generation Microscopy. *Opt. Lett.* **2011**, *36*, 3891-3893.

(13) Jang, J. H.; Jacob, J.; Santos, G.; Lee, T. R.; Baldelli, S. Image Contrast in Sum Frequency Generation Microscopy Based on Monolayer Order and Coverage. *J. Phys. Chem. C* **2013**, *117*, 15192-15202.

(14) Han, Y.; Raghunathan, V.; Feng, R.-r.; Maekawa, H.; Chung, C.-Y.; Feng, Y.; Potma, E. O.; Ge, N.-H. Mapping Molecular Orientation with Phase Sensitive Vibrationally Resonant Sum-Frequency Generation Microscopy. *J. Phys. Chem. B* **2013**, *117*, 6149-6156.

(15) Han, Y.; Hsu, J.; Ge, N.-H.; Potma, E. O. Polarization-Sensitive Sum-Frequency Generation Microscopy of Collagen Fibers. *J. Phys. Chem. B* **2015**, *119*, 3356-3365.

(16) Lee, C. M.; Kafle, K.; Huang, S.; Kim, S. H. Multimodal Broadband Vibrational Sum Frequency Generation (MM-BB-V-SFG) Spectrometer and Microscope. *J. Phys. Chem. B* **2016**, *120*, 102-116.

(17) Wang, H.; Gao, T.; Xiong, W. Self-Phase-Stabilized Heterodyne Vibrational Sum Frequency Generation Microscopy. *ACS Photonics* **2017**, *4*, 1839-1845.

(18) Hanninen, A.; Shu, M. W.; Potma, E. O. Hyperspectral Imaging with Laser-Scanning Sum-Frequency Generation Microscopy. *Biomed. Opt. Express* **2017**, *8*, 4230-4242.

(19) Huang, S.; Makarem, M.; Kiemle, S. N.; Hamedi, H.; Sau, M.; Cosgrove, D. J.; Kim, S. H. Inhomogeneity of Cellulose Microfibril Assembly in Plant Cell Walls Revealed with Sum Frequency Generation Microscopy. *J. Phys. Chem. B* **2018**, *122*, 5006-5019.

(20) Wang, H.; Chen, W.; Wagner, J. C.; Xiong, W. Local Ordering of Lattice Self-Assembled SDS@2β-CD Materials and Adsorbed Water Revealed by Vibrational Sum Frequency Generation Microscope. *J. Phys. Chem. B* **2019**, *123*, 6212-6221.

(21) Müller, N.; Buckup, T.; Motzkus, M. Flexible Pulse Shaping for Sum Frequency Microspectroscopies. *J. Opt. Soc. Am. B* **2020**, *37*, 117-126.

(22) Li, C.; Zhang, D.; Slipchenko, M. N.; Cheng, J.-X. Mid-Infrared Photothermal Imaging of Active Pharmaceutical Ingredients at Submicrometer Spatial Resolution. *Anal. Chem.* **2017**, *89*, 4863-4867.

(23) Pavlovetc, I. M.; Aleshire, K.; Hartland, G. V.; Kuno, M. Approaches to Mid-Infrared, Super-Resolution Imaging and Spectroscopy. *Phys. Chem. Chem. Phys.* **2020**, *22*, 4313-4325.

(24) Shi, J.; Wong, T. T. W.; He, Y.; Li, L.; Zhang, R.; Yung, C. S.; Hwang, J.; Maslov, K.; Wang, L. V. High-Resolution, High-Contrast Mid-Infrared Imaging of Fresh Biological Samples with Ultraviolet-Localized Photoacoustic Microscopy. *Nat. Photon.* **2019**, *13*, 609-615.

(25) Polli, D.; Kumar, V.; Valensise, C. M.; Marangoni, M.; Cerullo, G. Broadband Coherent Raman Scattering Microscopy. *Laser Photonics Rev.* **2018**, *12*, 1800020.

(26) Kano, H.; Segawa, H.; Okuno, M.; Leproux, P.; Couderc, V. Hyperspectral Coherent Raman Imaging - Principle, Theory, Instrumentation, and Applications to Life Sciences. *J. Raman Spectrosc.* **2015**, *47*, 116-123.

(27) Camp Jr, C. H.; Lee, Y. J.; Heddleston, J. M.; Hartshorn, C. M.; Walker, A. R. H.; Rich, J. N.; Lathia, J. D.; Cicerone, M. T. High-Speed Coherent Raman Fingerprint Imaging of Biological Tissues. *Nat. Photon.* **2014**, *8*, 627-634.

(28) Liao, C.-S.; Slipchenko, M. N.; Wang, P.; Li, J.; Lee, S.-Y.; Oglesbee, R. A.; Cheng, J.-X. Microsecond Scale Vibrational Spectroscopic Imaging by Multiplex Stimulated Raman Scattering Microscopy. *Light-Sci. Appl.* **2015**, *4*, e265.

(29) Shen, Y. R. *Fundamentals of Sum-Frequency Spectroscopy*; Cambridge University Press: Cambridge, 2016.

(30) Richmond, G. L. Molecular Bonding and Interactions at Aqueous Surfaces as Probed by Vibrational Sum Frequency Spectroscopy. *Chem. Rev.* **2002**, *102*, 2693-2724.

(31) Aric Opdahl; Telly, S. K.; Ella Amitay-Sadovsky; Joonyeong Kim; Somorjai, G. A. Characterization of Polymer Surface Structure and Surface Mechanical Behaviour by Sum Frequency Generation Surface Vibrational Spectroscopy and Atomic Force Microscopy. *J. Phys.: Condens. Matter* **2004**, *16*, R659.

(32) Wang, H.-F.; Gan, W.; Lu, R.; Rao, Y.; Wu, B.-H. Quantitative Spectral and Orientational Analysis in Surface Sum Frequency Generation Vibrational Spectroscopy (SFG-VS). *Int. Rev. Phys. Chem.* **2005**, *24*, 191-256.

(33) Yan, E. C. Y.; Fu, L.; Wang, Z.; Liu, W. Biological Macromolecules at Interfaces Probed by Chiral Vibrational Sum Frequency Generation Spectroscopy. *Chem. Rev.* **2014**, *114*, 8471-8498.

(34) Nihonyanagi, S.; Mondal, J. A.; Yamaguchi, S.; Tahara, T. Structure and Dynamics of Interfacial Water Studied by Heterodyne-Detected Vibrational Sum-Frequency Generation. *Annu. Rev. Phys. Chem.* **2013**, *64*, 579-603.

(35) Lu, X.; Zhang, C.; Ulrich, N.; Xiao, M.; Ma, Y.-H.; Chen, Z. Studying Polymer Surfaces and Interfaces with Sum Frequency Generation Vibrational Spectroscopy. *Anal. Chem.* **2017**, *89*, 466-489.

(36) Charan, K.; Li, B.; Wang, M.; Lin, C. P.; Xu, C. Fiber-Based Tunable Repetition Rate Source for Deep Tissue Two-Photon Fluorescence Microscopy. *Biomed. Opt. Express* **2018**, *9*, 2304-2311.

(37) Lévêque-Fort, S.; Papadopoulos, D. N.; Forget, S.; Balembois, F.; Georges, P. Fluorescence Lifetime Imaging with a Low-Repetition-Rate Passively Mode-Locked Diode-Pumped Nd:YVO$_4$ Oscillator. *Opt. Lett.* **2005**, *30*, 168-170.

(38) Chu, S.-W.; Liu, T.-M.; Sun, C.-K.; Lin, C.-Y.; Tsai, H.-J. Real-Time Second-Harmonic-Generation Microscopy Based on a 2-GHz Repetition Rate Ti:Sapphire Laser. *Opt. Exp.* **2003**, *11*, 933-938.

(39) Loza-Alvarez, P.; Brown, C. T. A.; Reid, D. T.; Sibbett, W.; Missey, M. High-Repetition-Rate Ultrashort-Pulse Optical Parametric Oscillator Continuously Tunable from 2.8 to 6.8 μm. *Opt. Lett.* **1999**, *24*, 1523-1525.

(40) Xu, B.; Wu, Y.; Sun, D.; Dai, H.-L.; Rao, Y. Stabilized Phase Detection of Heterodyne Sum Frequency Generation for Interfacial Studies. *Opt. Lett.* **2015**, *40*, 4472-4475.

(41) Pool, R. E.; Versluis, J.; Backus, E. H. G.; Bonn, M. Comparative Study of Direct and Phase-Specific Vibrational Sum-Frequency Generation Spectroscopy: Advantages and Limitations. *J. Phys. Chem. B* **2011**, *115*, 15362-15369.

(42) *Handbook of Optics. Volume IV, Optical Properties of Materials, Nonlinear Optics, Quantum Optics*; Bass, M.; Li, G.; Van Stryland, E. W., Eds.; McGraw-Hill: New York, 2010; Vol. 4.

(43) Chakraborty, I.; Pallen, S.; Shetty, Y.; Roy, N.; Mazumder, N. Advanced Microscopy Techniques for Revealing Molecular Structure of Starch Granules. *Biophys. Rev.* **2020**, *12*, 105-122.

(44) Buléon, A.; Colonna, P.; Planchot, V.; Ball, S. Starch Granules: Structure and Biosynthesis. *Int. J. Biol. Macromol.* **1998**, *23*, 85-112.

(45) Bertoft, E. Understanding Starch Structure: Recent Progress. *Agronomy* **2017**, *7*, 56.

(46) Waigh, T. A.; Hopkinson, I.; Donald, A. M.; Butler, M. F.; Heidelbach, F.; Riekel, C. Analysis of the Native Structure of Starch Granules with X-ray Microfocus Diffraction. *Macromolecules* **1997**, *30*, 3813-3820.

(47) Slepkov, A. D.; Ridsdale, A.; Pegoraro, A. F.; Moffatt, D. J.; Stolow, A. Multimodal CARS Microscopy of Structured Carbohydrate Biopolymers. *Biomed. Opt. Express* **2010**, *1*, 1347-1357.

(48) Kong, L.; Lee, C.; Kim, S. H.; Ziegler, G. R. Characterization of Starch Polymorphic Structures Using Vibrational Sum Frequency Generation Spectroscopy. *J. Phys. Chem. B* **2014**, *118*, 1775-1783.

(49) Wiercigroch, E.; Szafraniec, E.; Czamara, K.; Pacia, M. Z.; Majzner, K.; Kochan, K.; Kaczor, A.; Baranska, M.; Malek, K. Raman and Infrared Spectroscopy of Carbohydrates: A Review. *Spectrochim. Acta A* **2017**, *185*, 317-335.

(50) Longhi, G.; Zerbi, G.; Paterlini, G.; Ricard, L.; Abbate, S. Conformational Dependence of CH(CD)-Strechings in D-Glucose and Some Deuterated Derivatives as Revealed by Infrared and Raman Spectroscopy. *Carbohydr. Res.* **1987**, *161*, 1-22.

(51) Hieu, H. C.; Li, H.; Miyauchi, Y.; Mizutani, G.; Fujita, N.; Nakamura, Y. Wetting Effect on Optical Sum Frequency Generation (SFG) Spectra of D-Glucose, D-Fructose, and Sucrose. *Spectrochim. Acta A* **2015**, *138*, 834-839.

(52) Flores-Morales, A.; Jiménez-Estrada, M.; Mora-Escobedo, R. Determination of the Structural Changes by FT-IR, Raman, and CP/MAS $^{13}$C NMR Spectroscopy on Retrograded Starch of Maize Tortillas. *Carbohydr. Polym.* **2012**, *87*, 61-68.

(53) Zhang, L.; Fu, L.; Wang, H.-f.; Yang, B. Discovery of Cellulose Surface Layer Conformation by Nonlinear Vibrational Spectroscopy. *Sci. Rep.* **2017**, *7*, 44319.

(54) Kizil, R.; Irudayaraj, J.; Seetharaman, K. Characterization of Irradiated Starches by Using FT-Raman and FTIR Spectroscopy. *J. Agric. Food Chem.* **2002**, *50*, 3912-3918.

(55) Sevenou, O.; Hill, S. E.; Farhat, I. A.; Mitchell, J. R. Organisation of the External Region of the Starch Granule as Determined by Infrared Spectroscopy. *Int. J. Biol. Macromol.* **2002**, *31*, 79-85.

(56) Shoulders, M. D.; Raines, R. T. Collagen Structure and Stability. *Annu. Rev. Biochem.* **2009**, *78*, 929-958.

(57) Rocha-Mendoza, I.; Yankelevich, D. R.; Wang, M.; Reiser, K. M.; Frank, C. W.; Knoesen, A. Sum Frequency Vibrational Spectroscopy: The Molecular Origins of the Optical Second-Order Nonlinearity of Collagen. *Biophys. J.* **2007**, *93*, 4433-4444.

(58) Rivard, M.; Popov, K.; Couture, C.-A.; Laliberté, M.; Bertrand-Grenier, A.; Martin, F.; Pépin, H.; Pfeffer, C. P.; Brown, C.; Ramunno, L. et al. Imaging the Noncentrosymmetric Structural Organization of Tendon with Interferometric Second Harmonic Generation Microscopy. *J. Biophotonics* **2014**, *7*, 638-646.

(59) Hirose, C.; Akamatsu, N.; Domen, K. Formulas for the Analysis of the Surface SFG Spectrum and Transformation Coefficients of Cartesian SFG Tensor Components. *Appl. Spectrosc.* **1992**, *46*, 1051-1072.

(60) Berisio, R.; Vitagliano, L.; Mazzarella, L.; Zagari, A. Crystal Structure of the Collagen Triple Helix Model [(Pro-Pro-Gly)$_{10}$]$_3$. *Protein Sci.* **2002**, *11*, 262-270.

(61) Dow, X. Y.; DeWalt, E. L.; Sullivan, S. Z.; Schmitt, P. D.; Ulcickas, J. R. W.; Simpson, G. J. Imaging the Nonlinear Susceptibility Tensor of Collagen by Nonlinear Optical Stokes Ellipsometry. *Biophys. J.* **2016**, *111*, 1361-1374.

(62) Srivastava, S.; Srivastava, S.; Srivastava, S.; Shukla, M.; Gupta, V. D. Vibrational Dynamics of L-Proline-L-Hydroxyproline: A Fragment of Collagen. *J. Macromol. Sci. B* **2008**, *47*, 654-666.

(63) Hu, D.; Yang, Z.; Chou, K. C. Interactions of Polyelectrolytes with Water and Ions at Air/Water Interfaces Studied by Phase-Sensitive Sum Frequency Generation Vibrational Spectroscopy. *J. Phys. Chem. C* **2013**, *117*, 15698-15703.

(64) Yamamoto, K.; Kawaguchi, D.; Sasahara, K.; Inutsuka, M.; Yamamoto, S.; Uchida, K.; Mita, K.; Ogawa, H.; Takenaka, M.; Tanaka, K. Aggregation States of Poly(4-Methylpentene-1) at a Solid Interface. *Polym. J.* **2019**, *51*, 247-255.

(65) Orgel, J. P. R. O.; Sella, I.; Madhurapantula, R. S.; Antipova, O.; Mandelberg, Y.; Kashman, Y.; Benayahu, D.; Benayahu, Y. Molecular and Ultrastructural Studies of a Fibrillar Collagen from Octocoral (Cnidaria). *J. Exp. Biol.* **2017**, *220*, 3327.

(66) Rabotyagova, O. S.; Cebe, P.; Kaplan, D. L. Collagen Structural Hierarchy and Susceptibility to Degradation by Ultraviolet Radiation. *Mater. Sci. Eng. C* **2008**, *28*, 1420-1429.

(67) Tuer, A. E.; Krouglov, S.; Prent, N.; Cisek, R.; Sandkuijl, D.; Yasufuku, K.; Wilson, B. C.; Barzda, V. Nonlinear Optical Properties of Type I Collagen Fibers Studied by Polarization Dependent Second Harmonic Generation Microscopy. *J. Phys. Chem. B* **2011**, *115*, 12759-12769.

(68) Fechete, R.; Demco, D. E.; Blümich, B.; Eliav, U.; Navon, G. Anisotropy of Collagen Fiber Orientation in Sheep Tendon by $^1$H Double-Quantum-Filtered NMR Signals. *J. Magn. Reson.* **2003**, *162*, 166-175.

(69) Su, P.-J.; Chen, W.-L.; Chen, Y.-F.; Dong, C.-Y. Determination of Collagen Nanostructure from Second-Order Susceptibility Tensor Analysis. *Biophys. J.* **2011**, *100*, 2053-2062.

(70) York, R. L.; Holinga, G. J.; Somorjai, G. A. An Investigation of the Influence of Chain Length on the Interfacial Ordering of L-Lysine and L-Proline and Their Homopeptides at Hydrophobic and Hydrophilic Interfaces Studied by Sum Frequency Generation and Quartz Crystal Microbalance. *Langmuir* **2009**, *25*, 9369-9374.

(71) Holinga, G. J.; York, R. L.; Onorato, R. M.; Thompson, C. M.; Webb, N. E.; Yoon, A. P.; Somorjai, G. A. An SFG Study of Interfacial Amino Acids at the Hydrophilic SiO$_2$ and Hydrophobic Deuterated Polystyrene Surfaces. *J. Am. Chem. Soc.* **2011**, *133*, 6243-6253.

(72) Velarde, L.; Wang, H.-F. Unified Treatment and Measurement of the Spectral Resolution and Temporal Effects in Frequency-Resolved Sum-Frequency Generation Vibrational Spectroscopy (SFG-Vs). *Phys. Chem. Chem. Phys.* **2013**, *15*, 19970-19984.

(73) Richter, L. J.; Petralli-Mallow, T. P.; Stephenson, J. C. Vibrationally Resolved Sum-Frequency Generation with Broad-Bandwidth Infrared Pulses. *Opt. Lett.* **1998**, *23*, 1594-1596.

(74) Ji, N.; Ostroverkhov, V.; Chen, C.-Y.; Shen, Y.-R. Phase-Sensitive Sum-Frequency Vibrational Spectroscopy and Its Application to Studies of Interfacial Alkyl Chains. *J. Am. Chem. Soc.* **2007**, *129*, 10056-10057.

TOC graphic